

Article

A Novel Radar Cross-Section Calculation Method Based on the Combination of the Spectral Element Method and the Integral Method

Hongyu Zhao ^{1,†}, Jingying Chen ^{2,†}, Mingwei Zhuang ², Xiaofan Yang ¹ and Jianliang Zhuo ^{2,*} 

¹ State Key Laboratory of Complex Electromagnetic Environmental Effects on Electronics and Information System (CEMEE), Luoyang 471003, China

² Institute of Electromagnetics and Acoustics, Xiamen University, Xiamen 361005, China

* Correspondence: jianliangzhuo23@163.com or joybo@xmu.edu.cn

† These authors contributed equally to this work.

Abstract: This article proposes a novel method for calculating radar cross-sections (RCSs) that combines the spectral element method and the integral method, allowing for RCS calculations at any position in a free space or a half-space. This approach replaces the field source with an incident field using the scattered field equation of the spectral element method, enabling the arbitrary placement of the field source without being limited by the computational domain. By applying the superposition theorem and the volume equivalence principle, the scattered field of the objects at any position is obtained through integral equations, eliminating limitations on the computation points imposed by the computational domain. Based on Green's function's important role throughout the calculation process and its symmetry properties, the RCS calculation of symmetric models will be more advantageous. Finally, several examples, including symmetry models, are provided to validate both the feasibility and accuracy of this proposed method.

Keywords: radar cross-section (RCS); spectral element method (SEM); Green's function; integral method



Citation: Zhao, H.; Chen, J.; Zhuang, M.; Yang, X.; Zhuo, J. A Novel Radar Cross-Section Calculation Method Based on the Combination of the Spectral Element Method and the Integral Method. *Symmetry* **2024**, *16*, 542. <https://doi.org/10.3390/sym16050542>

Academic Editor: Nicolae Herisanu

Received: 25 January 2024

Revised: 22 March 2024

Accepted: 28 March 2024

Published: 1 May 2024



Copyright: © 2024 by the authors. Licensee MDPI, Basel, Switzerland. This article is an open access article distributed under the terms and conditions of the Creative Commons Attribution (CC BY) license (<https://creativecommons.org/licenses/by/4.0/>).

1. Introduction

A radar is a cutting-edge electronic device that utilizes electromagnetic waves for target detection, employing radio waves to ascertain the spatial location of targets through processes such as the emission, reflection, and scattering of electromagnetic waves. Due to its exceptional ability to penetrate space and minimal susceptibility to weather conditions, radar technology plays a pivotal role in military applications and finds extensive usage in critical civilian sectors [1]. However, with the continuous advancement of electronic information technology and the intense competition between stealth technology and anti-stealth technology in information warfare, radar systems face increasingly formidable challenges in detection and target identification [2,3].

A radar cross-section (RCS) serves as a crucial technical indicator for radar systems by quantifying the power returned from a target when illuminated by plane waves at specific angles. The RCS depends not only on factors like incident electromagnetic wave frequency, propagation direction, and polarization mode but also on target morphology, size, material parameters, as well as scattering direction influence. It holds significant importance for radar system design, stealth design, and the analysis of target scattering characteristics. Nevertheless, accurately modeling and calculating the RCS of a target remains an arduous task demanding substantial computational resources. Generally speaking, it can be achieved through experimental measurements or numerical calculations; however, experimental measurements entail not only complete radar systems but also vast measurement sites, whereas numerical calculation methods offer advantages such as low

resource consumption and shorter cycle times, making them widely applied in today's rapidly developing era of computer science.

Nowadays, various methods have been developed in numerical computation techniques, including analytical methods, integral methods, and differential methods. Analytical methods start with the fluctuation equation and calculate the analytical solution of the field based on the boundary conditions of the scattering target. They are primarily suitable for simple models. Yucedag et al. (2014) presented an analytical method for calculating the monostatic RCS of a perfectly conducting wind turbine model located over a dielectric lossy half-space [4]. Ates et al. (2021) improved the calculation of the electromagnetic scattering from deformed spherical conducting objects [5]. When employing integral techniques for calculating the RCS, the discretization of the region of interest is typically accomplished through the utilization of Green's functions. The most common method used in integral equations is the method of moments (MOM) [6–8], which is suitable for targets of an arbitrary geometry with arbitrary source excitation and is highly precise when solving scattering problems. Luente et al. (2008) utilized an iteration-free MOM approach to solve large multiscale electromagnetic scattering problems [9]. Lee et al. (2022) used MOM to quickly estimate the dynamic RCS of a drone in various motions [10]. Differential methods generally require boundary conditions to truncate open spaces and can theoretically handle various shapes and parameterized media situations. Ozgun and Kantartzis (2019) presented a high-fidelity full-wave simulator for solving the problem of 2D electromagnetic scattering over a 1D sea surface [11]. Ohtani et al. (2021) applied the nonstandard finite-difference time-domain (NS-FDTD) technique to assess the overall RCS evaluation of various aircraft configurations with an electrically large size [12].

Although analytical methods can achieve a high accuracy with fewer resources, their effectiveness is limited to simple models. Integral methods can handle complex models, but they face challenges in solving high-contrast scattering problems due to their dense matrices. In addition, MOM is more suitable for small targets during the solving process, as it needs to consume a lot of memory. Despite the emergence of some improved algorithms such as the characteristic basis method of moment (CBMOM), the convergence of numerical results is still difficult to achieve systematically [9,13]. The multilayer fast multipole method (MLFMM), which combines MOM and fast algorithms, improves the computational speed of MOM and also reduces memory consumption. However, it still takes a long time to compute, and the limitation of storage remains its bottleneck [14]. On the other hand, differential methods like the finite-difference time-domain (FDTD) [15,16], the finite-volume time-domain (FVTD) [17–19], the finite element method (FEM) [7,20,21], and the spectral element method (SEM) [22–27] can effectively address high-contrast problems but have a limitation, according to which both the source and receiver points must be within the computational domain. This paper introduces a novel approach in which SEM is integrated with the integral method to establish a set of efficient, accurate, and versatile RCS calculation techniques applicable to arbitrary targets in a free space or layered media.

This paper is organized as follows: in Section 2, we derive the SEM based on the control equations of the incident and scattered fields. The scattered field integral equation, combined with the superposition theorem and volume equivalence principle, is employed to determine the scattered field at any desired location. Finally, the RCS at any position exposed to an arbitrary field source can be rapidly ascertained through the definition of the RCS. In Section 3, the feasibility and accuracy of this method are incrementally validated through three numerical examples conducted in either free-space or half-space environments. In the concluding section, definitive conclusions and future prospects are presented.

2. Methods

A typical RCS calculation model is shown in Figure 1, which depicts a detection system consisting of a radiation source in the air and a receiving device on the ground for detecting a specific target on the ground. In this section, we initially employ incident fields instead of

emission sources to derive the electromagnetic field at any position within the computational domain. Subsequently, SEM is used to solve the equation for the scattered field at any location within the computational region, and the scattered field integral equation is utilized to compute the scattered field at any location outside the calculation domain. Considering the crucial role played by Green's functions in this process, we further introduce Green's functions. Ultimately, the RCS at any given location is determined via its definition.

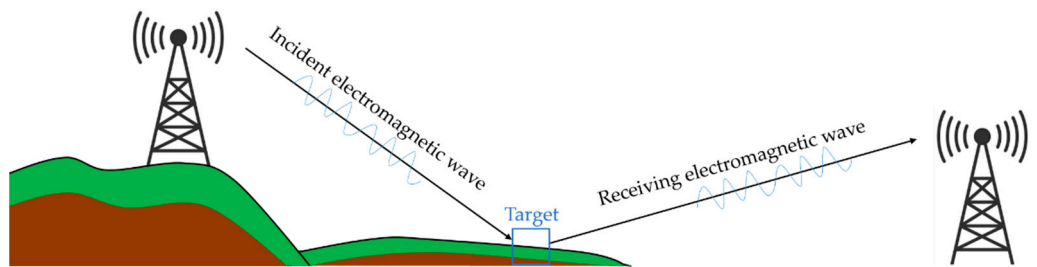


Figure 1. A typical RCS calculation model.

2.1. SEM

In order to derive the SEM based on the control equations for the incident and scattered fields, the first step is the vector Helmholtz equation for the magnetic field:

$$-\nabla \times \left(\bar{\epsilon}_r^{-1} \nabla \times \mathbf{H}^t \right) + k_0^2 \bar{\mu}_r \mathbf{H}^t = -\nabla \times \left(\bar{\epsilon}_r^{-1} \mathbf{J} \right) \quad (1)$$

where $\bar{\epsilon}_r = \bar{\epsilon}_r + \bar{\sigma}_r / j\omega$; $\bar{\epsilon}_r$, $\bar{\sigma}_r$, and $\bar{\mu}_r$ represent the permittivity, conductivity, and permeability, respectively; ω is the angular frequency; k_0 is the number of waves in the vacuum; \mathbf{H}^t is the total magnetic field; and \mathbf{J} is the current density.

Assuming the absence of a scatterer in the background field, Equation (1) represents the control equation for the background field and can be expressed as

$$-\nabla \times \left(\bar{\epsilon}_b^{-1} \nabla \times \mathbf{H}^i \right) + k_0^2 \bar{\mu}_b \mathbf{H}^i = -\nabla \times \left(\bar{\epsilon}_b^{-1} \mathbf{J} \right) \quad (2)$$

where $\bar{\epsilon}_b = \bar{\epsilon}_r + \bar{\sigma}_r / j\omega$; $\bar{\epsilon}_b$, $\bar{\sigma}_b$, and $\bar{\mu}_b$ represent the permittivity, conductivity, and permeability of the background medium, respectively; and \mathbf{H}^i is the incident magnetic field.

By subtracting Equation (3) from Equation (2) and applying the electromagnetic field's superposition theorem ($\mathbf{H}^s = \mathbf{H}^t - \mathbf{H}^i$), followed by substituting it with the volume equivalence principle, the vector Helmholtz equations that pertain to the incident and scattered magnetic fields are obtained:

$$\nabla \times \left(\bar{\epsilon}_r^{-1} \nabla \times \mathbf{H}^s \right) - k_0^2 \bar{\mu}_r \mathbf{H}^s = j\omega \epsilon_0 \nabla \times \left(\mathbf{I} - \bar{\epsilon}_b \bar{\epsilon}_r^{-1} \right) \mathbf{E}^i + k_0^2 \left(\bar{\mu}_r - \bar{\mu}_b \right) \mathbf{H}^i \quad (3)$$

where \mathbf{H}^s is the scattered magnetic field, \mathbf{E}^i represents the incident electric field, ϵ_0 is the relative permittivity in vacuum, \mathbf{I} is the unit vector, and ω is the angular frequency.

For solving the scattered field problem in three-dimensional electromagnetic fields, Equation (3) can be employed as the governing equation for the SEM method [28]. This approach enables the direct derivation of the scattered field within the computational region when the incident field is known.

To enhance the convenience and streamline the calculation, this paper employs the GLL basis function, which offers overlapping interpolation and integration points [29].

Additionally, the Galerkin weighted residual method is utilized to improve computational accuracy. Hence, a discrete linear system can be obtained as follows:

$$\begin{pmatrix} \mathbf{S} - k_0^2 \mathbf{M} & \mathbf{K} \\ \mathbf{K}^T & 0 \end{pmatrix} \begin{pmatrix} \mathbf{x} \\ \mathbf{y} \end{pmatrix} = \begin{pmatrix} \mathbf{b} \\ \mathbf{c}_a \end{pmatrix} \quad (4)$$

where \mathbf{S} is the stiffness matrix, \mathbf{M} is the mass matrix, \mathbf{K} is the constraint matrix, \mathbf{K}^T is the transpose of \mathbf{K} , vectors \mathbf{x} and \mathbf{y} denote the unknowns of \mathbf{H}^s and the Lagrange multiplier \mathbf{p} , respectively, and \mathbf{b} and \mathbf{c}_a are the source terms corresponding to the right-hand sides of Equation (3). The exact derivation and expression of the formula can be found in [28]. Consequently, as the order of the basis function increases, the interpolation error of SEM decreases exponentially, resulting in exponential convergence and a significantly reduced computational effort. The distinguishing feature of SEM lies in its fusion of the finite element method and the spectral method, leveraging the spectral accuracy and geometric flexibility within grid cells. By solving Equation (3) for a scattered field within the scatterer and superimposing it with the incident field, the rapid determination of the total field at any position inside the scatterer can be achieved.

2.2. Scattered Fields' Integral Equations

The scattered fields' integral equations are based on the principle of electromagnetic field superposition and the theory of volume equivalence. The total strength of the electromagnetic field is the combination of the incident and scattered fields through the principle of superposition. The scattered field is linked to the total field through the body equivalent source, forming the volume equivalence theorem with the total field as the unknown quantity. When considering the scattered field beyond the confines of the computational region, this study applies the volume equivalence principle and the superposition theorem to derive the secondary scattered field of the scattering object through the integral equation of the scattered field.

Based on the volume equivalence theorem, the scattered field can be equivalently represented as a field generated by equivalent sources within the scatterers. The relationships between the total field $\mathbf{E}^t(\mathbf{r})$ and $\mathbf{H}^t(\mathbf{r})$ and the equivalent electric current source \mathbf{J}_{eq} and the equivalent magnetic current source \mathbf{M}_{eq} can be expressed as follows:

$$\mathbf{J}_{eq} = j\omega\epsilon_0 \left(\bar{\bar{\epsilon}}(\mathbf{r}) - \bar{\bar{\epsilon}}_b \right) \mathbf{E}^t(\mathbf{r}) \quad (5)$$

$$\mathbf{M}_{eq} = j\omega\mu_0 \left(\bar{\bar{\mu}}(\mathbf{r}) - \bar{\bar{\mu}}_b \right) \mathbf{H}^t(\mathbf{r}) \quad (6)$$

where $\bar{\bar{\epsilon}}(\mathbf{r})$ and $\bar{\bar{\mu}}(\mathbf{r})$ represent the permittivity tensor and permeability tensor at position \mathbf{r} in space, respectively. In accordance with the superposition principle, the scattered field at any location \mathbf{r} can be derived by convolving the equivalent source with its Green function:

$$\mathbf{E}^s(\mathbf{r}) = \int_V \bar{\bar{G}}_{EJ}(\mathbf{r}, \mathbf{r}') \mathbf{J}_{eq}(\mathbf{r}') d\mathbf{r} + \int_V \bar{\bar{G}}_{EM}(\mathbf{r}, \mathbf{r}') \mathbf{M}_{eq}(\mathbf{r}') d\mathbf{r} \quad (7)$$

$$\mathbf{H}^s(\mathbf{r}) = \int_V \bar{\bar{G}}_{HJ}(\mathbf{r}, \mathbf{r}') \mathbf{J}_{eq}(\mathbf{r}') d\mathbf{r} + \int_V \bar{\bar{G}}_{HM}(\mathbf{r}, \mathbf{r}') \mathbf{M}_{eq}(\mathbf{r}') d\mathbf{r} \quad (8)$$

where $\bar{\bar{G}}_{EJ}(\mathbf{r}, \mathbf{r}')$, $\bar{\bar{G}}_{HJ}(\mathbf{r}, \mathbf{r}')$, $\bar{\bar{G}}_{EM}(\mathbf{r}, \mathbf{r}')$, and $\bar{\bar{G}}_{HM}(\mathbf{r}, \mathbf{r}')$ represent Green's functions originating from the equivalent sources \mathbf{J}_{eq} and \mathbf{M}_{eq} located from \mathbf{r}' to \mathbf{r} . From Equation (4) to Equation (8), it can be seen that, when the total fields $\mathbf{E}^t(\mathbf{r})$ and $\mathbf{H}^t(\mathbf{r})$ are determined, the scattered field at any position \mathbf{r} can be quickly obtained by combining Green's function.

2.3. Green's Function

A complex source can be decomposed into a combination of unit sources. If the field generated by each unit source can be determined, then the field generated by any

source under the same boundary conditions can be obtained through the superposition principle. The field generated by unit sources is called Green's function, which elucidates the relationship between an excitation source and the excitation field. The proposed method for calculating radar cross-sections (RCSs) in this article involves multiple applications of Green's function to solve the corresponding electromagnetic field problems. Specifically, within the spectral element method, the incident field from the excitation source to the scattering object needs to be computed using Green's function. In order to determine the scattered field through integral equations, it is essential to solve the equation with Green's function from an equivalent source to a receiving point. Furthermore, when subsequently calculating the RCS, it is also necessary to employ Green's functions to obtain the incident field from the excitation source to the receiving point.

Given the focus of this paper on addressing vector field solutions, dyadic Green functions (DGF) are employed to establish a connection between vector fields and vector sources [30]. DGF manifests distinct forms in different background media, with an analytical solution applicable in free space and a semi-analytical solution utilized in planar layered media. In this study, the transmission line equations serve as the primary approach for solving DGF in layered media [31]. Initially, the Fourier transform is applied to the xoy plane to derive expressions for any field component. Subsequently, the Helmholtz equation for point sources is transformed into a solution involving transmission line equations and transmission line Green functions (TLGF). This transformation enables us to obtain spectral-domain solutions for electric and magnetic fields. Finally, by employing the inverse Fourier transform, spatial-domain DGFs can be inferred.

As demonstrated in the previous two sections, Green's functions play a crucial role in both of these computational processes. The SEM utilizes the incident field obtained through Green's functions to replace the excitation source, effectively solving the problem of a limited calculation domain for the excitation source. On the other hand, Green's functions in integral equations of scattered fields address the issue of a restricted calculation domain for the field points. Consequently, Green's functions effectively integrate the SEM and the scattered field integration method, thereby significantly reducing the calculation domain to solely encompassing the vicinity of the scattering object's surface. This achievement successfully minimizes computational resource consumption while enhancing the overall efficiency.

2.4. RCS Calculation Method

Based on Green's function, the scattered field and incident field at the corresponding position can be rapidly determined utilizing the methodologies presented in the preceding subsections. Subsequently, the specific value σ can be further derived using the RCS formula:

$$\sigma = -4\pi R^2 \frac{|\mathbf{E}^s|^2}{|\mathbf{E}^i|^2} \quad (9)$$

where R is the distance from the observation point to the detected target. In practical applications, the RCS is commonly represented in a logarithmic form. If the scattering target is far away from both the transmitting source and the receiving radar, significantly exceeding the incident wavelength and size of the scatterer, it can be treated as a point scatterer. In this case, the incident electromagnetic wave illuminating the surface of the scatterer can be approximated as a plane wave. Equation (9), defining the RCS, remains applicable.

3. Experiment

According to the novel RCS calculation method discussed above, this section presents three numerical cases to progressively assess the feasibility and accuracy of the proposed approach. The first case initially verifies the accuracy of the SEM method, followed by the second case which confirms the accuracy of the integration method, and, finally, the third case corroborates the accuracy of the RCS calculation. To validate the result accuracy

when the excitation sources are located outside the computational domain, traditional SEM and commercial software results are used as the reference values, with an electric dipole employed as the excitation source. Due to limited computational resources, reduced models are utilized in these numerical examples. The SEM in all the examples employs perfectly matched layers as the boundary conditions for the purpose of delineating the open space. All the simulations are performed on a workstation with a 40-core Xeon Gold 6230 2.1 GHz CPU and 512 GB RAM.

3.1. The Scattered Field Based on the SEM

This case is designed in free space, with a geometric model symmetric along the $x = 0$ plane, as shown in Figure 2a. The computational domain has dimensions of $0.66 \text{ m} \times 0.66 \text{ m} \times 0.20 \text{ m}$ and is centered at the origin. Two scatterers with dimensions of $0.30 \text{ m} \times 0.6 \text{ m} \times 0.10 \text{ m}$ are positioned at coordinates $(0.15, 0, 0) \text{ m}$ and $(-0.15, 0, 0) \text{ m}$, respectively. An electric dipole serves as the excitation source operating at a frequency of 2 GHz with the polarization $(1, 1, 1)$ and is situated at $(0.0, 0.2, 0.16) \text{ m}$. A uniform array consisting of observation points measuring $120 \times 120 \times 20$ is distributed within the scatterers. The electromagnetic parameters of the background medium are $\bar{\epsilon}_b = 1$, $\bar{\sigma}_b = 10^{-6} \text{ s/m}$, and $\bar{\mu}_b = 1$, and the electromagnetic parameters of the scatterer are $\bar{\epsilon}_{r1} = 6$, $\bar{\sigma}_{r1} = 5 \times 10^{-3} \text{ s/m}$, $\bar{\mu}_{r1} = 2$ and $\bar{\epsilon}_{r2} = 4$, $\bar{\sigma}_{r2} = 10^{-3} \text{ s/m}$, and $\bar{\mu}_{r2} = 2$.

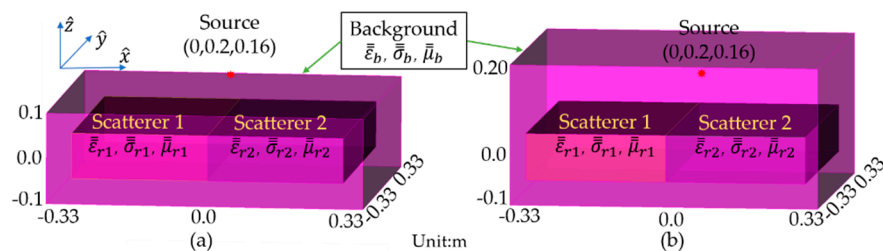


Figure 2. The model for case 1: (a) the model for SEM based on the scattered field's governing equation; (b) the model for SEM based on the total field's governing equation.

For comparison, traditional SEM is employed. The excitation source is included in the calculation area of the comparison model, as shown in Figure 2b. Therefore, the size of the calculation area becomes $0.66 \text{ m} \times 0.66 \text{ m} \times 0.3 \text{ m}$, with a center position at $(0, 0, 0.05) \text{ m}$, while the other parameters remain consistent with those in Figure 2a. The commercial software COMSOL is also used as a comparison. After conducting numerous experiments, we have carefully selected a relatively optimal calculation area measuring $0.90 \text{ m} \times 0.90 \text{ m} \times 0.3 \text{ m}$ in size. Additionally, we have applied a perfectly matched layer with a thickness of 0.15 m as the boundary condition.

Due to the inherent limitations of traditional SEM or COMSOL in directly calculating the scattered field, a two-step approach is required for comparing the scattering fields: first, by directly computing the total field; and second, by substituting the scatterer with a background medium to determine the incident field. Consequently, the scattered field can be obtained as the difference between the total field and the incident field. The comparison of the scattered fields inside the scatterer for two different SEM methods and COMSOL is illustrated in Figure 3, where "SEM 1" denotes the proposed method, and "SEM 2" represents the conventional SEM. The x -axis represents randomly selected observation points, which are part of a total of 288,000 observation points. It is evident from Figure 3 that both methods yield highly consistent results. Additionally, the unrepresented components (E_z , H_x , and H_y) demonstrate an equivalent level of accuracy. The discrepancy between

the different methods is further quantified by calculating the L2-norm errors, which are given by the following equation:

$$\text{L2 norm error} = \frac{\|R_A - R_B\|_2}{\|R_A\|_2} \quad (10)$$

where R stands for electric or magnetic field, A is the traditional SEM or COMSOL, and B is the proposed method. Specifically, the L2 norm error between two different SEM is 0.13% for the electric field and 0.1% for the magnetic field; meanwhile, the L2 norm error between SEM1 and COMSOL is 0.58% for the electric field and 0.54% for the magnetic field. In SEM1, it requires 719 s of CPU time and utilizes 127 GB of memory to acquire the scattered field, whereas, in SEM2 and COMSOL, it takes 1356 s and 3340 s, respectively, to obtain the total field within the computational domain. Additionally, it consumes 161 GB and 366 GB of memory, correspondingly.

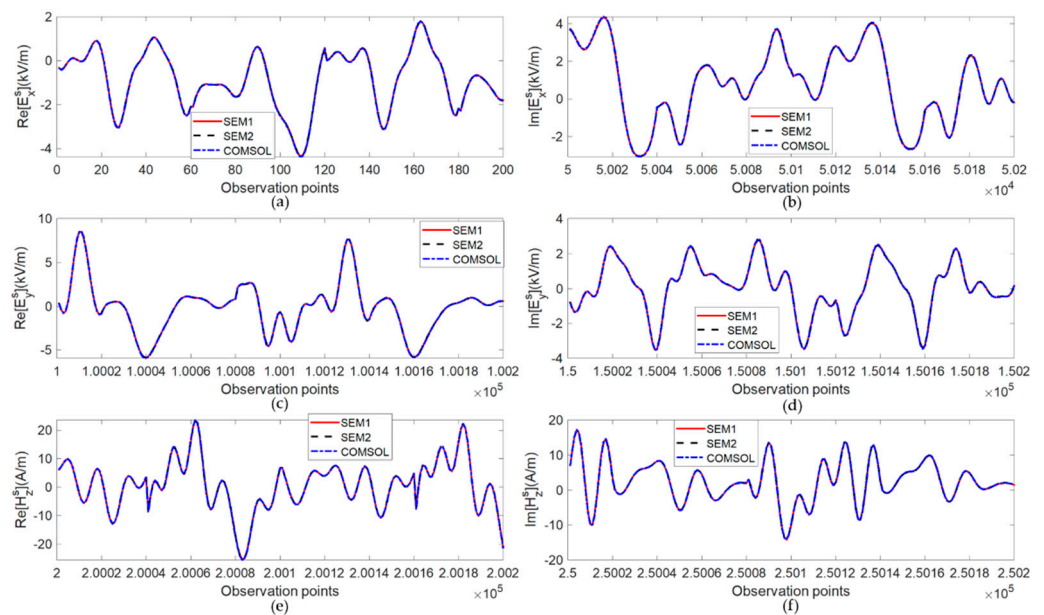


Figure 3. The comparison of the scattered fields inside the scatterer for two different SEM methods and COMSOL. (a,b) Real and imaginary parts of the x -component electric fields, respectively. (c,d) Real and imaginary parts of the y -component electric fields, respectively. (e,f) Real and imaginary parts of the z -component magnetic fields, respectively.

3.2. The Scattered Field Based on the Integral Method

The present case investigates a model in a half-space, as illustrated in Figure 4. The upper half-space represents the air, while the lower half-space represents the ground. The scatterer with the dimensions of $0.06 \text{ m} \times 0.06 \text{ m} \times 0.02 \text{ m}$ is positioned on the ground surface and centered at the origin. The model in Figure 4a (named model A) has a computational domain size of $0.12 \text{ m} \times 0.12 \text{ m} \times 0.08 \text{ m}$, where the ground height is set to 0.05 m, and the underground depth is set to be 0.03 m. Given its inclusion of excitation sources within the computational domain, this model is well-suited for COMSOL, and, in the actual simulation, a perfectly matched layer with a 0.015 m thickness is attached to the outer surface of this computational domain as the boundary condition. The model in Figure 4b (named model B), however, does not incorporate an excitation source within its computational domain of a $0.07 \text{ m} \times 0.07 \text{ m} \times 0.03 \text{ m}$ size and, thus, possesses slightly larger dimensions than the scatterer. Both the ground height and the underground depth are reduced to 0.025 m and 0.005 m, respectively. Also, it suits the method proposed in this paper. The electromagnetic parameters of the background medium are $\bar{\epsilon}_{b1} = 1$,

$\bar{\sigma}_{b1} = 10^{-6}$ s/m, and $\bar{\mu}_{b1} = 1$ and $\bar{\sigma}_{b2} = 4$, $\bar{\sigma}_b = 10^{-4}$ s/m, and $\bar{\mu}_b = 1$, and the electromagnetic parameters of the scatterer are $\bar{\epsilon}_r = 3$, $\bar{\sigma}_r = 10^{-3}$ s/m, and $\bar{\mu}_r = 1$.

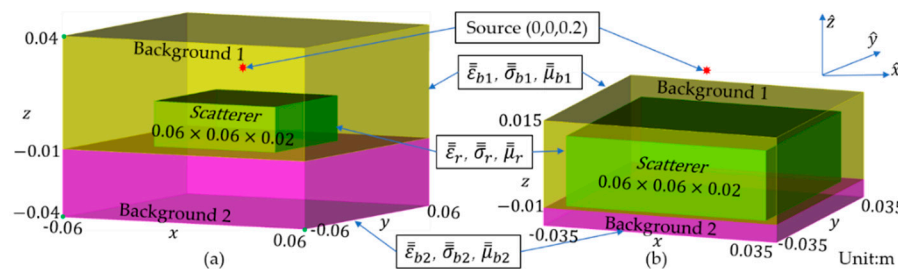


Figure 4. The model for case 2: (a) the model for COMSOL; (b) the model for the proposed method where the source is outside the computational domain.

The excitation source with polarization $(1, 1, 1)$ is located at $(0.0, 0.0, 0.03)$ m and operates at a frequency of 10 GHz. For the purpose of convenient comparison, the observation points are set within the computational domain of model A and without that of model B. Therefore, when considering the experimental design, the observation points are placed on the $z = 0.038$ m plane.

According to the volume equivalence theorem, the scatterer is discretized into uniformly sized small cubic cells with dimensions of $60 \times 60 \times 20$. Each cell has a size smaller than a 0.1 wavelength, allowing it to be considered an equivalent source. By employing SEM and applying the superposition principle of the electromagnetic field, we can determine the total field at the center of each cell. Subsequently, integral equations are used to calculate the scattered field at any given position. After comparison, Figure 5 illustrates the contrasting results of the total field strength inside the scatterer, while Figure 6 presents the contrasting results of the scattered field strength at observation points external to the scatterer. It is evident from these two figures that different methodologies yield consistent electromagnetic fields both inside and outside the scatterer. To quantify these discrepancies, the L2 norm error is also employed to assess their accuracy. Within the internal region of the scatterer, the L2 norm errors are 0.78% and 0.74% for the electric field strength and magnetic field strength obtained by the two methods, respectively, whereas, at observation points external to the scatterer, there are L2 norm errors of 0.54% and 0.46%, respectively. In terms of computational efficiency, the SEM requires 855 s to complete the calculation and utilizes 110 GB of memory, whereas COMSOL necessitates 2979 s and consumes 310 GB of memory.

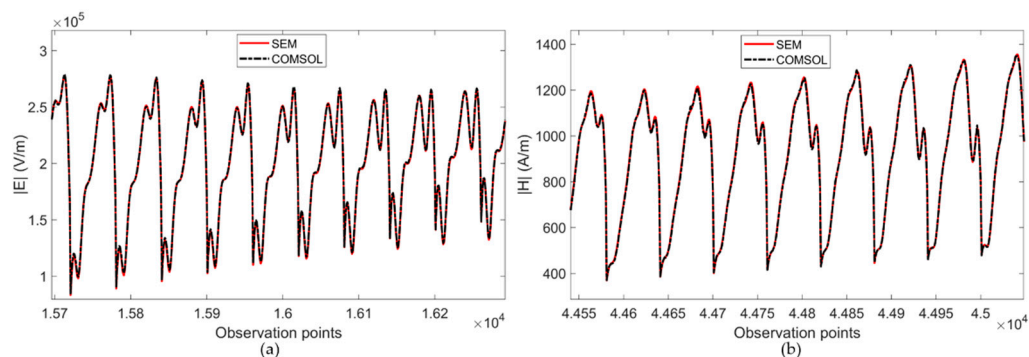


Figure 5. The comparison of the total field strength inside the scatterer for SEM and COMSOL: (a) the comparison of the electric field strength; (b) the comparison of the magnetic field strength.

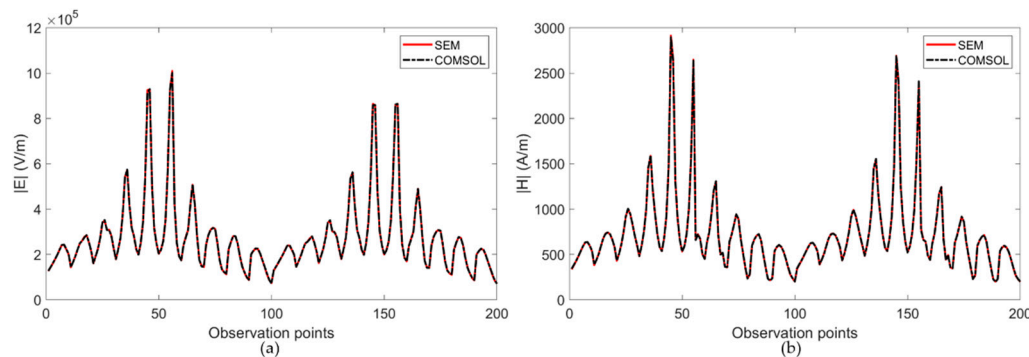


Figure 6. The comparison of the scattered field strength at observation points external to the scatterer for SEM and COMSOL: **(a)** the comparison of the electric field strength; **(b)** the comparison of the magnetic field strength.

3.3. Validation of RCS Calculation in Free Space

Due to the inability of existing commercial software to directly calculate the RCS under high-contrast, hierarchical models, a cuboid model in free space was employed to evaluate the accuracy of our proposed method for RCS calculation. The obtained results were compared with those obtained using FEKO, a widely-used commercial software. As shown in Figure 7, the cuboid scatterer, measuring $0.5 \text{ m} \times 0.5 \text{ m} \times 0.1 \text{ m}$, is positioned in free space with its body center serving as the origin. The electromagnetic properties of both the background medium and the scatterer are represented by $\bar{\epsilon}_b = 1$, $\bar{\sigma}_b = 10^{-6} \text{ s/m}$, and $\bar{\mu}_b = 1$ and $\bar{\epsilon}_r = 3$, $\bar{\sigma}_r = 10^{-3} \text{ s/m}$, and $\bar{\mu}_r = 1$, respectively. The electric dipole, polarized along the $(1, 1, 1)$ direction and operating at a frequency of 2 GHz, is positioned at a high altitude of $(0, 0, 150 \text{ m})$ to ensure an appropriate distance from the target. The observation points are positioned at a distance of 30 m from the origin, with a pitch angle θ of 60° . The azimuth angle φ varies from 0° to 360° in increments of 1° , resulting in a total of 361 points. The size of the computational domain for the spectral element method is set to $0.54 \text{ m} \times 0.54 \text{ m} \times 0.14 \text{ m}$, as there is no necessity to include the source and observation points.

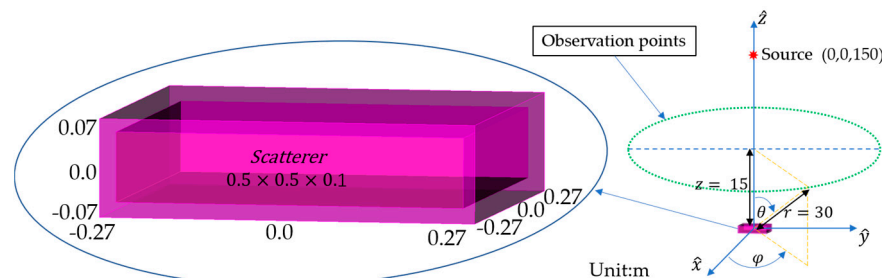


Figure 7. Schematic model of a cuboid scatterer in free space.

The comparison between the calculation of the proposed method and the FEKO result is shown in Figure 8, where logarithmic expressions are used to facilitate the intuitive display of the RCS results at each point. The figure highlights that the RCS calculation method proposed in this paper matches FEKO's results, indicating that this method can accurately calculate the RCS of target scatterers. The error is further quantified by Equation (10), where R represents the RCS value, subscripts A and B represent FEKO and the proposed method, respectively, and the L2-norm error resulting from the two methods of calculation is 3.7%. The error is slightly larger compared to the first two cases, which may be due to the fact that the FEKO calculation method in this model is based on the integral equation method. The accuracy and stability of the numerical integration may be slightly affected when dealing with scattering problems with a high contrast. Nevertheless, the results still show a very high accuracy. This better illustrates that the method presented in this paper

effectively addresses the issue of high-contrast scattering while maintaining a high level of accuracy.

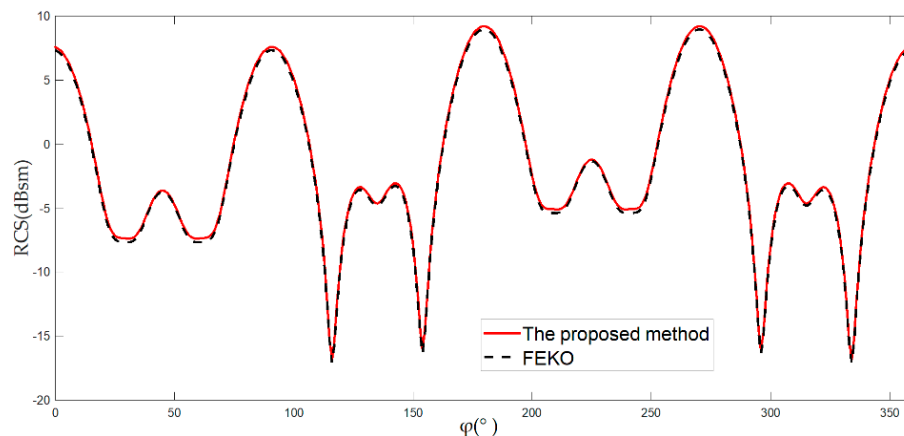


Figure 8. The RCS comparison between the proposed method and FEKO.

4. Conclusions

The proposed method for calculating RCS combines the SEM with integral equations. In the SEM part, an incident field is utilized instead of an excitation source, reducing the computational domain and resource consumption while expanding its applicability. In the integral equation part, by mapping SEM results to equivalent sources and combining them with Green's functions, the effective computation of scattered fields at any spatial position can be achieved, overcoming limitations regarding SEM's computation domain and further extending its application scope. Finally, RCS's values can be easily determined through its definition. Subsequently, three numerical examples are presented to gradually verify the feasibility and accuracy of this proposed method.

In conventional differential methods, the computation of electromagnetic fields necessitates placing field sources and field points within the computational domain, resulting in an expansion of the computation region and consequently consuming more computational resources. This paper proposes an innovative approach that confines the computation domain to the proximity of the target of interest, thereby significantly reducing the demand for computational resources. Consequently, with equivalent computational resources, this method enables the more accurate simulation of electromagnetic field scattering from larger targets of interest. Moreover, this method is not only applicable to calculating the radar cross-section (RCS) for airborne targets but also ground targets.

The method proposed in this paper demonstrates significant theoretical innovation and engineering applicability, while still allowing for further enhancements when confronted with more intricate background media. We eagerly anticipate future research endeavors in this domain.

Author Contributions: Conceptualization, H.Z., X.Y. and J.Z.; methodology, J.C. and J.Z.; software, M.Z. and J.Z.; validation, H.Z., J.C. and J.Z.; writing—original draft preparation, H.Z. and J.C.; writing—review and editing, J.Z. All authors have read and agreed to the published version of the manuscript.

Funding: This research received no external funding.

Data Availability Statement: The data used in the experiment are detailed in the experiment section.

Conflicts of Interest: The authors declare no conflict of interest.

References

- Hou, Y.; Ren, H.; Lv, Q.; Wu, L.; Yang, X.; Quan, Y. Radar-Jamming Classification in the Event of Insufficient Samples Using Transfer Learning. *Symmetry* **2022**, *14*, 2318. [[CrossRef](#)]
- Li, G.; Wang, L.; Wu, G.; Zhou, G. Multiframe Track-Before-Detect of Weak Fluctuating Targets in a Complex-Valued RD Plane. *Symmetry* **2022**, *14*, 2357. [[CrossRef](#)]
- Quan, D.; Tang, Z.; Wang, X.; Zhai, W.; Qu, C. LPI Radar Signal Recognition Based on Dual-Channel CNN and Feature Fusion. *Symmetry* **2022**, *14*, 570. [[CrossRef](#)]
- Yucedag, S.M.; Yucedag, O.M.; Serim, H.A. Analytical method for monostatic radar cross section calculation of a perfectly conducting wind turbine model located over dielectric lossy half space. *IET Radar Sonar Navig.* **2014**, *8*, 965–970. [[CrossRef](#)]
- Ates, B.; Kustepeli, A.; Cetin, Z. Analytical Improvement on the Electromagnetic Scattering From Deformed Spherical Conducting Objects. *IEEE Trans. Antennas Propag.* **2021**, *69*, 8630–8640. [[CrossRef](#)]
- Harrington, R.F. *Field Computation by Moment Methods*; Oxford University Press, Inc.: Oxford, UK, 1993; p. 240. [[CrossRef](#)]
- Paknys, R. *Applied Frequency-Domain Electromagnetics*; John Wiley & Sons Press: Hoboken, NJ, USA, 2016. [[CrossRef](#)]
- Wang, S.G.; Guan, X.P.; Wang, D.W.; Ma, X.Y.; Su, Y. Electromagnetic scattering by mixed conducting/dielectric objects using higher-order MOM. *Prog. Electromagn. Res.* **2006**, *66*, 51–63. [[CrossRef](#)]
- Lucente, E.; Monorchio, A.; Mittra, R. An Iteration-Free MoM Approach Based on Excitation Independent Characteristic Basis Functions for Solving Large Multiscale Electromagnetic Scattering Problems. *IEEE Trans. Antennas Propag.* **2008**, *56*, 999–1007. [[CrossRef](#)]
- Lee, D.Y.; Lee, J.I.; Seo, D.W. RCS Estimation of Drone Motion Using Mesh-Element Rotation in MoM and Micro-Doppler Signatures. *IEEE Trans. Antennas Propag.* **2022**, *70*, 7344–7349. [[CrossRef](#)]
- Ozgun, O.; Kuzuoglu, M. A Domain Decomposition Finite-Element Method for Modeling Electromagnetic Scattering From Rough Sea Surfaces With Emphasis on Near-Forward Scattering. *IEEE Trans. Antennas Propag.* **2019**, *67*, 335–345. [[CrossRef](#)]
- Ohtani, T.; Kanai, Y.; Kantartzis, N.V. Partial RCS Evaluation Method for Low-Observable Aircraft Design using PEC and PMC Boundaries. In Proceedings of the 2021 International Applied Computational Electromagnetics Society Symposium (aces), Hamilton, ON, Canada, 1–5 August 2021.
- Tchikaya, E.B.; Khalil, F.; Tahir, F.A.; Aubert, H. Multi-Scale Approach for the Electromagnetic Simulation of Finite Size and Thick Frequency Selective Surfaces. *Prog. Electromagn. Res. M* **2011**, *17*, 43–57. [[CrossRef](#)]
- Potgieter, M. Bistatic RCS calculations of complex realistic targets using asymptotic methods. In Proceedings of the 2018 International Workshop on Computing, Electromagnetics, and Machine Intelligence (CEMi), Stellenbosch, South Africa, 21–24 November 2018; pp. 23–24.
- Taflove, A. *Computational Electrodynamics: The Finite-Difference Time-Domain Method*; Artech House: Norwood, MA, USA, 1995; p. 599.
- Yee, K.S. Numerical solution of initial boundary value problems involving Maxwell's equations in isotropic media. *IEEE Trans. Antennas Propag.* **1966**, *14*, 302–307. [[CrossRef](#)]
- Madsen, N.K.; Ziolkowski, R.W. A Three-Dimensional Modified Finite Volume Technique for Maxwell's Equations. *Electromagnetics* **1990**, *10*, 147–161. [[CrossRef](#)]
- Shankar, V.; Mohammadian, A.H.; Hall, W.F. A Time-Domain, Finite-Volume Treatment for the Maxwell Equations. *Electromagnetics* **1990**, *10*, 127–145. [[CrossRef](#)]
- Fedeli, A.; Pastorino, M.; Randazzo, A. A Hybrid Asymptotic-FVTD Method for the Estimation of the Radar Cross Section of 3D Structures. *Electronics* **2019**, *8*, 1388. [[CrossRef](#)]
- Courant, R. Variational methods for the solution of problems of equilibrium and vibrations. *Bull. Am. Math. Soc.* **1943**, *49*, 1–24. [[CrossRef](#)]
- Holand, I. The Finite Element Method in Plane Stress Analysis. *Finite Elem. Methods Stress Anal.* **1960**, *43*–92.
- Patera, A.T. A Spectral Element Method for Fluid-Dynamics—Laminar-Flow in a Channel Expansion. *J. Comput. Phys.* **1984**, *54*, 468–488. [[CrossRef](#)]
- Fornberg, B. *A Practical Guide to Pseudospectral Methods*; Cambridge University Press: Cambridge, UK, 1996; pp. 167–169. [[CrossRef](#)]
- Joon-Ho, L.; Tian, X.; Liu, Q.H. A 3-D spectral-element method using mixed-order curl conforming vector basis functions for electromagnetic fields. *IEEE Trans. Microw. Theory Tech.* **2006**, *54*, 437–444. [[CrossRef](#)]
- Liu, J.; Jiang, W.; Liu, N.; Liu, Q.H. Mixed Spectral-Element Method for the Waveguide Problem with Bloch Periodic Boundary Conditions. *IEEE Trans. Electromagn. Compat.* **2019**, *61*, 1568–1577. [[CrossRef](#)]
- Wang, J.; Li, J.; Liu, J.; Liu, Q.H. Spectral-Element Spectral-Integral (SESI) Method for the 1-D Bloch (Floquet) Periodic Problems With Scatterers Embedded in Multiple Regions of 2-D Layered Media. *IEEE Trans. Microw. Theory Tech.* **2022**, *70*, 1006–1015. [[CrossRef](#)]
- You, L.; Yan, K.; Liu, N.; Shi, T.; Lv, S. Assessing the mechanical responses for anisotropic multi-layered medium under harmonic moving load by Spectral Element Method (SEM). *Appl. Math. Model.* **2019**, *67*, 22–37. [[CrossRef](#)]
- Huang, T.; Zhuang, M.; Zhuo, J.; Hong, R.; Sun, Y.; Liu, Q.H. Mixed Spectral Element Method for Electromagnetic Secondary Fields in Stratified Inhomogeneous Anisotropic Media. *IEEE Access* **2021**, *9*, 218–225. [[CrossRef](#)]
- Liu, N.; Cai, G.; Zhu, C.; Tang, Y.; Liu, Q.H. The Mixed Spectral-Element Method for Anisotropic, Lossy, and Open Waveguides. *IEEE Trans. Microw. Theory Tech.* **2015**, *63*, 3094–3102. [[CrossRef](#)]

30. Eroglu, A.; Lee, Y.H.; Lee, J.K. Dyadic Green's functions for multi-layered uniaxially anisotropic media with arbitrarily oriented optic axes. *IET Microw. Antennas Propag.* **2011**, *5*, 1779–1788. [[CrossRef](#)]
31. Michalski, K.A.; Mosig, J.R. Multilayered Media Green's Functions in Integral Equation Formulations. *IEEE Trans. Antennas Propag.* **1997**, *45*, 508–519. [[CrossRef](#)]

Disclaimer/Publisher's Note: The statements, opinions and data contained in all publications are solely those of the individual author(s) and contributor(s) and not of MDPI and/or the editor(s). MDPI and/or the editor(s) disclaim responsibility for any injury to people or property resulting from any ideas, methods, instructions or products referred to in the content.